Open access • Journal Article • DOI:10.1088/1361-6501/AA8DBF

On the metrology of interparticle contacts in sand from x-ray tomography images

Max Wiebicke, Max Wiebicke, Edward Andò, Ivo Herle ...+1 more authors

Institutions: Dresden University of Technology, University of Grenoble

Published on: 22 Nov 2017 - Measurement Science and Technology (IOP Publishing)

Topics: Contact area

On the metrology of interparticle contacts in sand from x-ray tomography images

Max Wiebicke, Edward Andò, Ivo Herle, Gioacchino Viggiani

On the metrology of interparticle contacts in sand from x-ray tomography images

Max Wiebicke[a,b], Edward Andò[a], Ivo Herle[b], Gioacchino Viggiani[a]

[a] *Univ. Grenoble Alpes, CNRS, Grenoble INP[1], 3SR, F-38000 Grenoble, France*
[b] *Institute of Geotechnical Engineering, Technische Universität Dresden, D-01062 Dresden, Germany*

Abstract

In the mechanics of granular materials, interparticle contacts play a major role. These have been historically difficult to study experimentally, but the advent of x-ray micro tomography allows the identification of all the thousands of individual particles needed for representative mechanical testing. This paper studies the metrology of detecting interparticle contacts and measuring their orientation from such images.

Using synthetic images of spheres, and high-resolution tomographies of two very different granular materials (spherical and very angular) as ground truths we find that these measurements are far from trivial. For example, if a physically-correct threshold is used to separate particles from pores there is a *systematic over-detection* of contacts. We propose a method of improvement that is effective for non-angular particles.

When contact orientations are measured from the pixels that make up the contact area, standard watershed approaches make significant systematic errors. We confirm and build upon previous results showing the improvement in orientation measurement using a refined notion of particle separation. Building on this solid basis, future work should focus on a link between contact topology and measurement error, as well as evaluating the use of local surface normals for orientation measurement.

1. Introduction

Granular Materials and fabric. Among the many peculiar features of the mechanical behaviour of granular materials, the pronounced change of stiffness upon load reversal is an excellent example of a well known phenomenon which is difficult to explain. A standard mechanical test to investigate this change upon load reversal is depicted in Figure 1. The macroscopic response of a natural sand is plotted on the left of the Figure; in order to investigate the stiffness change the specimen is loaded (01-03), then unloaded (03-04) and reloaded (04-05). The fundamental reason for the enormous change in stiffness reflects a change in the way forces are transmitted through the system at the contact points between the particles. However, this does not require or cause a large rearrangement of the granular skeleton. This means that the origin of the stiffness evolution is somehow encoded in the change of *geometry* of the granular skeleton, commonly referred to as *fabric*. In literature, fabric is often described as a tensorial quantity calculated from a) the position and orientation of inter-particle contacts and/or b) the orientation of grains themselves and/or c) the orientation of voids in between the particles [1, 2].

Image Analysis. This article develops and characterises the performance of image analysis tools to measure inter-granular contact orientation (a. above) from mechanical tests on granular materials performed within an x-ray tomograph. This means that a number of different 3D images of a deforming specimen are acquired in the course of loading and load reversal. The performance of the proposed measurement tools is characterised with respect to both a) a numerically-generated ground truth using the recently published Kalisphera [3] tool, and b) a "golden standard" in the form of very high resolution x-ray tomography scans of the grains in question.

[1] Institute of Engineering Univ. Grenoble Alpes

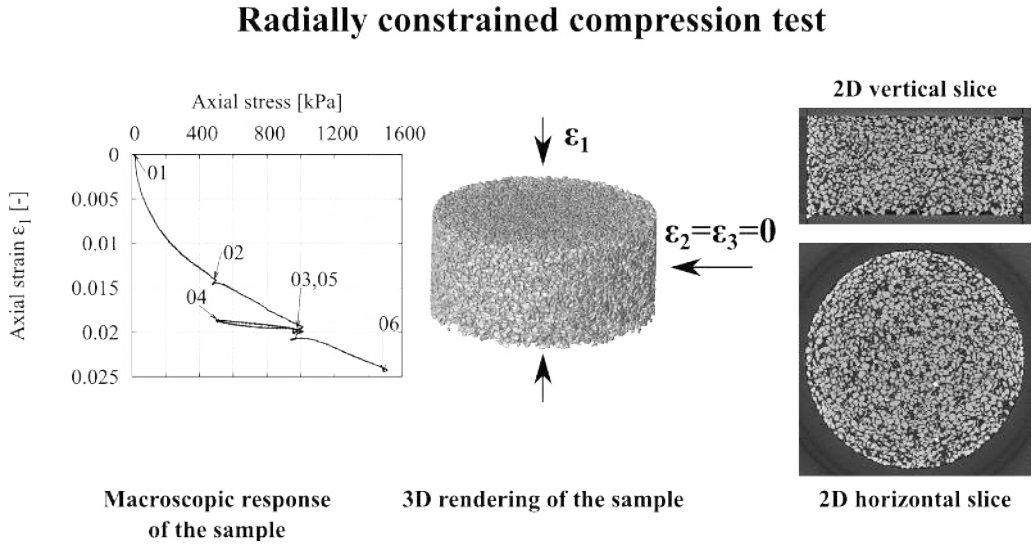

Figure 1: A standard experiment in soil mechanics – the radially constrained compression test of a natural sand.

Resolution trade-off. In lab-based x-ray tomography using a divergent x-ray beam, there is a well-known trade-off between the resolution of the image and the field of view [4]. Practically speaking, for a given particle size (around 300 μm in our case), one must choose between images that include a few grains at a high resolution and a larger number of grains at lower resolution. Since the driving question of the stiffness upon load reversal pertains to the macroscopic response of the material, this imposes a granular assembly of sufficient size to have a representative mechanical response. Based on previous work, we have selected a specimen size of 22 mm height and 11 mm diameter which contains several tens of thousands of grains, meaning that at a pixel size of 10-15 μm/px there are more than 10 pixels across each grain diameter in the 3D images acquired during the test. Standard image processing tools are known not to give satisfactory results on inter-particle contacts; this is proved, and improved techniques are proposed [5].

State of the art of segmentation techniques. The aim of this work is not to provide a thorough study across many different segmentation techniques, but rather to present a procedure to assess the accuracy of a chosen image analysis technique. As described in [6] among many other publications [7, 8, 9], there exist a variety of different segmentation techniques, for example: global and local thresholding, region growing methods, deformable surfaces (such as level sets), probabilistic clustering or Bayesian methods. In [6], the focus is on porous materials (such as granular materials) and it was found that none of the techniques that were tested performed without problems – only two global thresholds (Otsu [10] and Ridler) and most of the local thresholds yielded satisfactory results (the local thresholds, however, being sensitive to the initial input).

Other segmentation methods were developed to target specific granular materials, which implies an a-priori knowledge of the shape: [11] worked on spheres and [12] on mono-sized spheres and cylindrical containers. However, as these methods are limited to specific shapes and often uniform particles, they cannot be applied to natural granular materials. Furthermore, the problem of the detection of contacts was highlighted in [11]. For an approach consisting of a global threshold followed by a standard watershed, they concluded that [*... even a minor error in the choice of the binarization threshold can ... make the detection going completely wrong.*] The quantification of this error is one of the main aims of this contribution.

As mentioned above, level sets can also be used to describe particle morphology and inter-particle contacts in granular materials as shown in [13]. However, this approach also relies on an initial segmentation to serve as an input to determine the level sets of each individual particle.

[14] provides one of the rare studies on the quantification of the accuracy of μ-CT regarding porous materials. Therein, microscopy is used as a "golden standard" and the accuracy is assessed by matching binarised μ-CT slices (2D images) with binarised microscopic images (serving as the ground truth) of the same section. This study concludes that using a global threshold to analyse μ-CT images, 11% of the total amount of voxels are visualised wrongly – meaning that solid voxels are wrongly declared as void voxels and vice-versa.

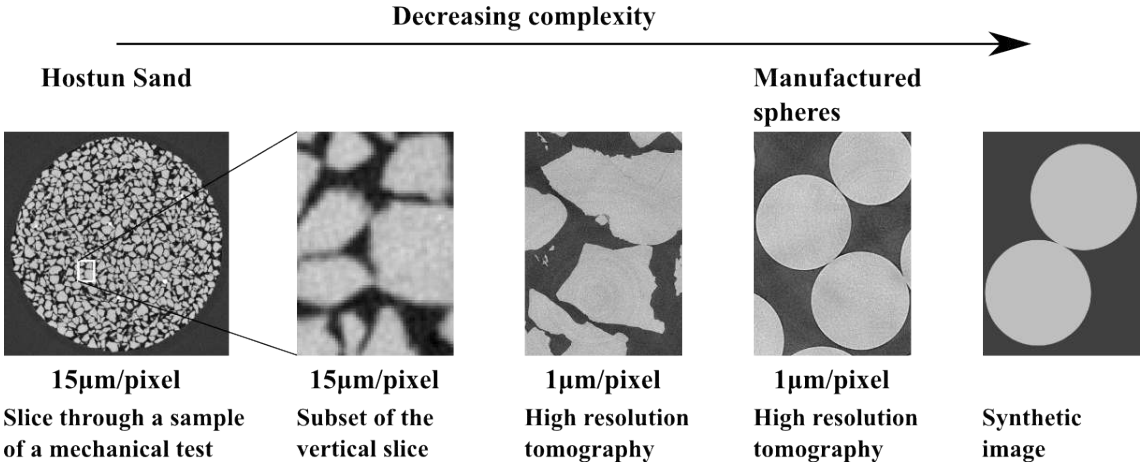

Figure 2: Strategy to approach this analysis. Simplifying tomographic images of a natural sand at standard resolution for mechanical testing by acquiring high resolution tomographic images and degrading the shape to spheres.

The main problems of the segmentation of CT images are found to be the partial volume effect, noise and blur (among others that however can mostly be dealt with by special filtering [7]). Thus, our analysis mainly focuses on these inherent problems. As global thresholding and standard topological watersheds represent the most commonly used techniques in the mechanics of granular materials, we chose to quantify their accuracy regarding the determination of contact properties.

General introduction to our approach. In order to conduct an analysis of the accuracy of different, but standard tools to determine contact properties from x-ray tomographic images, we adopt the following approach where we gradually increase complexity, see Figure 2: Synthetic images of spheres, that are created in a way to reproduce the partial volume effect, serve as the basis for the analysis, because all of the investigated contact properties are known beforehand from the analytical solution of touching spheres (the so-called "branch vector" that links the centres of two touching spheres has the same orientation as their contact). Furthermore, we bypass the well-known problem of lacking the ground truth in tomography images [6] by using synthetic images of spheres where every detail is imposed and known. To get closer to real tomographic images, these spheres are blurred and noise is added in subsequent steps of this study. Thereafter, real shapes are added from high resolution x-ray images of two different granular materials: The first material investigated using the high resolution images consists of high-precision manufactured ruby spheres, for which again the contact orientation is approximately known. The second material is a natural sand called Hostun sand, for which there is no analytical solution for the positions and orientations of the grain contacts.

2. Measurement of contact properties with artificial images

2.1. Generation of controlled artificial images

We select to start working on spheres, because the location of the contact points and the orientation of the contact planes can be determined analytically if the positions of the spheres are known. The contact orientation is defined as the normal to the contact plane at which two particles are touching each other. It coincides with the orientation of the branch vector of these particles, which is the vector that connects the centres of these spheres.

This motivates the use of Kalisphera [3] to generate synthetic images of spheres for which we know the ground truth. Furthermore, Kalisphera reproduces the partial volume effect when creating the images of spheres, which is of utmost importance in this analysis. The first part of the analysis is done on Kalisphera images, which are created with 32bit floating point values, where 0.25 defines a pure void voxel and 0.75 a pure solid voxel, with any value between 0.25 and 0.75 representing a partially filled voxel[2]. In order to get closer to tomographic images, blur and noise

[2]0.25 and 0.75 are chosen rather than the more standard 0.0 and 1.0 in order to leave room to add noise and keep the values between 0.0 and 1.0

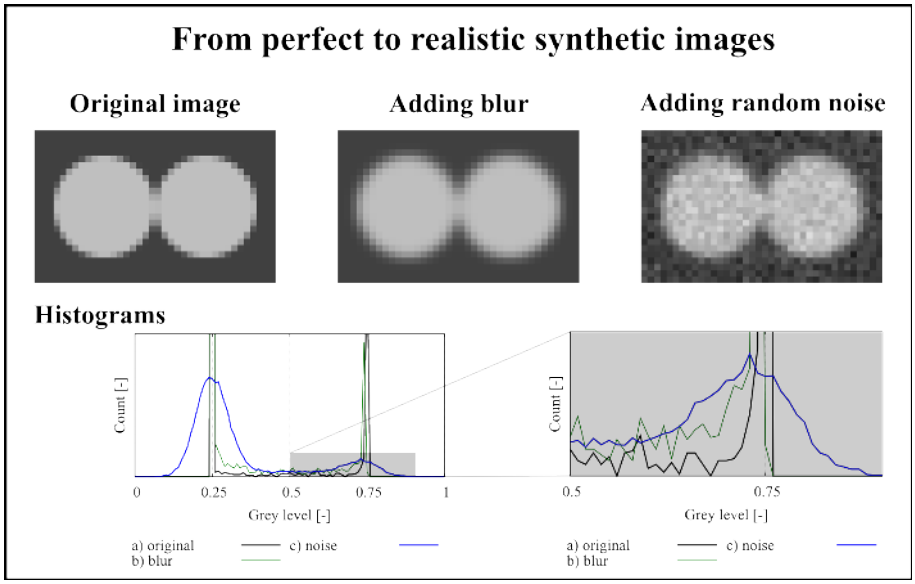

Figure 3: Illustration of the method to generate controlled realistic images from Kalisphera images by blurring and adding random noise.

are then added to the images.

Blur is added directly to the images using Kalisphera, where a Gaussian blur operator is applied to the generated spheres. The level of the blur is being specified by the standard deviation, with the objective of reproducing the overall point-spread-function of an x-ray imaging system, including the reconstruction of the 3D.

Introduction of noise. The controlled addition of blur is not sufficient to create a synthetic image with the same defects as x-ray tomography since noise is present in the 3D images reconstructed from x-ray radiographies. In x-ray radiography, where photons are being (often indirectly) counted, a combination of Poisson and Gaussian noise can be expected. Still, experience shows that Gaussian noise is a good approximation for the result of image reconstruction (see Figure 4b). Therefore we add Gaussian noise – *i.e.,* a random variation based on a Gaussian distribution – to our blurred Kalisphera images.

The method to reproduce, in controlled conditions, the different defects of tomographic images is presented in Figure 3. Slices of the three-dimensional image of two touching spheres are shown for every step described above: from the original image to a blurred image and finally to a noisy image. The histograms that are plotted in Figure 3 for every image illustrate the process of simulating real tomographic images: the histogram of the perfect image tends to two singular values at 0.25 for the void phase and 0.75 for the solid phase, whereas the final image, to which blur and noise were applied, tends to a wider histogram that is comparable to histograms of real tomographies.

In order to calibrate the noise that has to be added to the synthetic images, representative tomographic images are taken as a reference. Figure 4 shows the image of a granular assembly during a mechanical test at a pixel size of 10 μm/pixel. Typically, these images are reconstructed as 16-bit integer images, but for comparison they are converted to 32-bit float images and the grey values are translated such that the mean values of the solid and the void phases are ≈ 0.75 and 0.25, respectively. The noise manifests in the standard deviations of the solid σ_s and the void phase σ_v of the histogram. These standard deviations in the presented image are $\sigma_s = 0.021$ and $\sigma_v = 0.028$. Images of another mechanical test at a pixel size of 15 μm/pixel confirmed these image characteristics.

Reference set of configurations. In order to investigate different configurations of two spheres, a reference set of 5,000 orientations is defined and used as a reference set of branch vectors between particle centres. The reference set is shown as a Lambert azimuthal equal-area projection in Figure 5. All analyses on artificial images are conducted on this reference set.

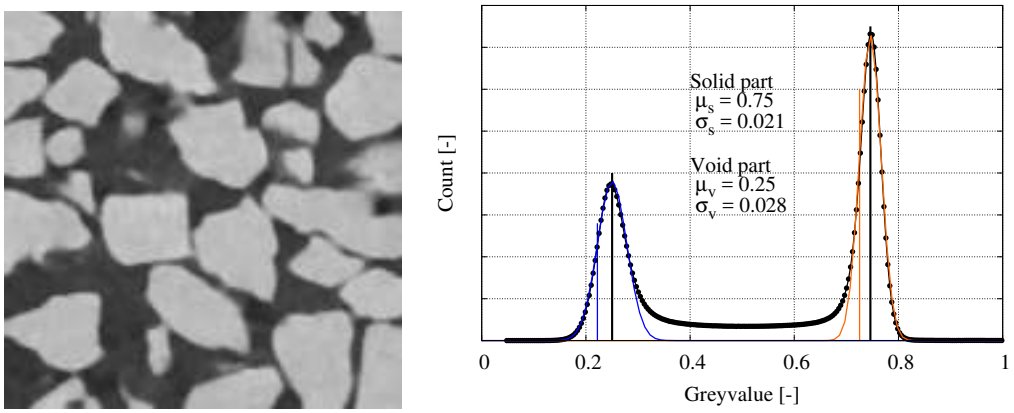

(a) Slice of a tomographic image

(b) Histogram of the tomographic image

Figure 4: Characterisation of noise: a) small subset of the original 3D tomography of a representative mechanical test at a pixel size of 10 μm/pixel b) Histogram of the 3D image, rescaled to yield the mean values of solid and void part at 0.75 and 0.25, respectively.

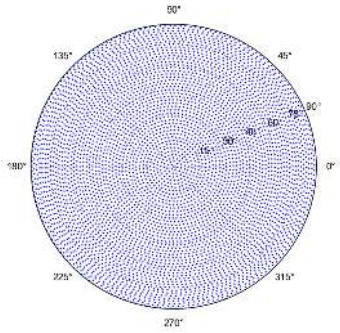

Figure 5: Lambert azimuthal equal-area projection of the imposed orientations

2.2. Contact detection

In this section we will be dealing with the detection of a possible contact between two spheres. The first step for the detection of this contact is the binarisation of the greyscale image to unequivocally distinguish the solid and void phases. A threshold for the binarisation can be found using various approaches. It is generally based either on the statistics of the image (*e.g.*, Otsu's threshold [10]), or on a physical calibration: in experiments the overall mass of the tested material is usually known and can be used to determine this threshold provided that the density of the particles is known. The threshold used for the binarisation is called **global** threshold hereafter.

For Kalisphera images, the global threshold that yields the correct volume of the spheres for their imposed radius is a greylevel of 0.5, which selects the more-than-half-filled partial volume voxels. In case of rigid spheres, the contact must theoretically correspond to a single point. When an artificial image is created of two spheres that touch, the application of the global threshold yields a solid voxelised connection between the two particles, since each sphere partially intrudes into the voxels around the contact point as illustrated in Figure 6. Given the solid connection between the two particles, they are considered to be in contact. Therefore when the partial volume "aura" of each sphere overlaps, this makes a single solid object.

Unfortunately, even when the spheres are generated in such a way that they have a non-zero distance at their closest point (*i.e.,* no contact), the partial volume effects of both spheres are combined such that the global threshold identifies a solid bridge between the particles. This is demonstrated in Figure 6 where the particles have a distance of 1 pixel between them. The conclusion is that a physically-correct global threshold gravely overestimates the number of touching spheres in a 3D image for an assembly of spheres, due to the additive nature of the partial volume effect.

In order to assess up to which distance the separated spheres still appear to be in contact, we conduct the following analysis on our reference set of 5,000 branch vector orientations between

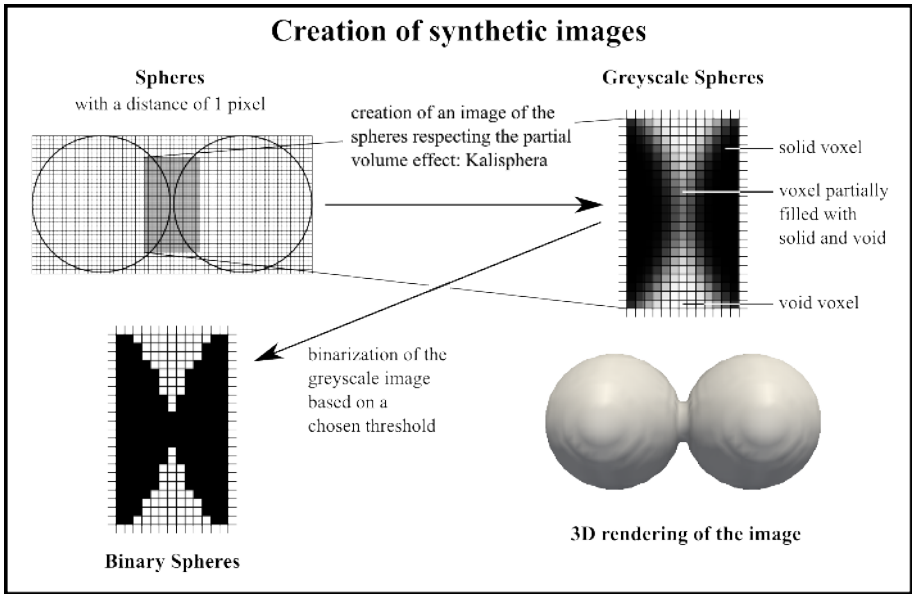

Figure 6: Illustration of the creation of Kalisphera sphere and the partial volume effect.

two spheres: The analysis is initialised setting the distance between two particles to 0 pixels, *i.e.*, the particles are touching in one point. This distance is then increased in small increments until the spheres no longer appear to touch after application of the global threshold of 0.5. A standard squared connectivity equal to one is used to check whether one (spheres in contact) or two (spheres separated) objects appear in the binarised image; *i.e.,* a 3x3x3 object with all but the diagonal components being 1. The blue line (blur=0.0) in Figure 7 shows the results of this analysis for all 5000 orientations. It is obvious that the application of a physically-correct threshold on these images leads to a systematic *over-detection distance* of interparticle contacts.

Note that using digital-image correlation, granular kinematics can be measured with a precision significantly higher than 0.1 pixels [15], so the over-detection of contacts for up to 1 pixel separation is a serious problem.

After increasing the distance of the spheres to more than 0.3 pixels (dependent on the configuration), the spheres start to appear separated, but up to a distance of 1 pixel, contacts might still be detected for some special orientations. For the sake of completeness, an enhanced connectivity of only ones (3x3x3 object with all components equal 1) was assessed as well to detect contacts and results in substantially higher errors.

Adding blur. Carrying out this analysis for different levels of Gaussian blurring results in larger errors, meaning that spheres will appear to be in contact for even larger distances: see the green and the red lines in Figure 7. A representative level of blur for the x-ray CT scanner in Laboratoire 3SR for the experimental conditions of interest in this study is 0.8 [3]. Consequently, only this level of blur is considered for the subsequent analysis within this paper. The results presented here are obtained creating spheres with a diameter of 30 pixels, but importantly are scale independent, *i.e.,* changing the size of the spheres changes the results only negligibly.

Local refinement. In order to reduce the systematic over-detection in interparticle contacts, we propose the following refinement: After thresholding with the global threshold, the contact area is extracted as a subset of the image. A higher threshold, which will be called **local threshold**, is applied on the subset to check whether the contact still exists. In order to calibrate the local threshold, the same analysis as above is conducted with different local thresholds being applied to the images in each step. The effect on the *over-detection distance* between two particles, for all orientations, and for different thresholds is presented in Figure 8 – solid lines. Increasing the local threshold leads to a decrease of the *over-detection distance* that was found using the standard

[3]The value of Gaussian blur of 0.8 for the Laboratoire 3SR system comes from the Kalisphera "sphere matching" procedure detailed in [3] leaving the blur as a free variable to optimise on the analysis of tomographic images of spheres acquired in similar conditions to the ones that will be used in experiments

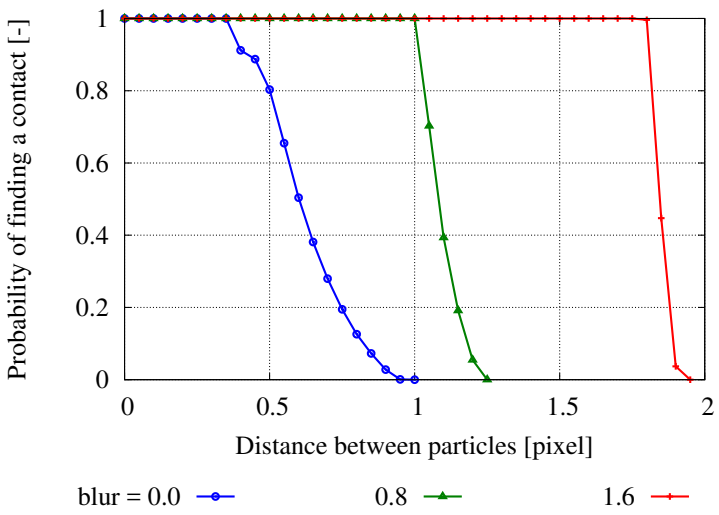

Figure 7: Results of the contact detection study on Kalisphera spheres (diameter = 30 pixels) using a physically correct global threshold of 0.5.

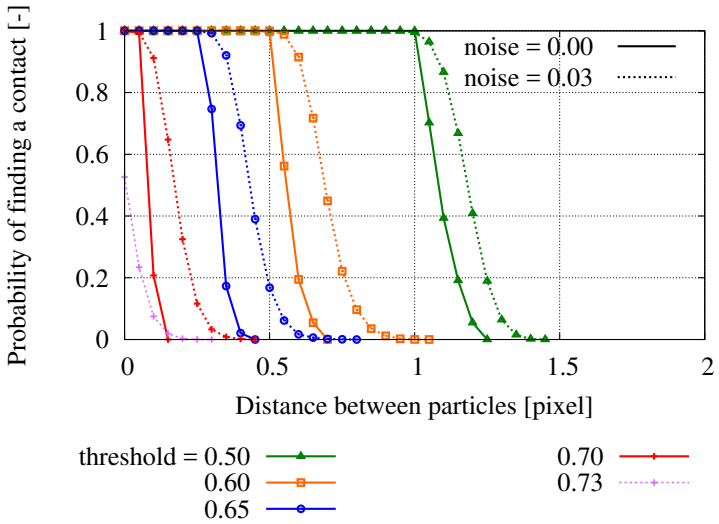

Figure 8: Results of the contact detection study on Kalisphera spheres (diameter = 30 pixels) using a global threshold of 0.5. Applying different local thresholds on images created with a blur of 0.8. Results are shown for noiseless images (solid lines), and for images with additive Gaussian noise std=0.03 (dashed lines)

approach (green line, similar to Figure 7). The best results are found at a local threshold of 0.65, where we start loosing contacts at a distance larger than 0.1 pixels. However, care must be taken for local thresholds higher than 0.70 which eventually lead to a loss of contacts: the solid line corresponding to a local threshold of 0.73 is absent in Figure 8.

Introducing noise. A representative level of noise for the images of interest for this study has been found – by fitting two Gaussian curves to the greylevel distributions of solids and voids – to be a standard deviation of around 0.03 for both, compare to Figure 4b.

This level of random noise is therefore added to the blurred images, and its effect on the *over-detection distance* is presented in Figure 8 – dashed lines. Comparing solid and dashed lines of the same colour, it is evident that on average this level of noise increases the *over-detection distance*, degrading the quality of the measurement. As before, applying a local threshold reduces *over-detection distance*.

A conclusion on threshold. It emerges from the above discussion on contact detection that with a physically-correct threshold, the number of grain-to-grain contacts in a granular assembly is *systematically* overestimated. The concept of the *over-detection distance* is key in this case – a

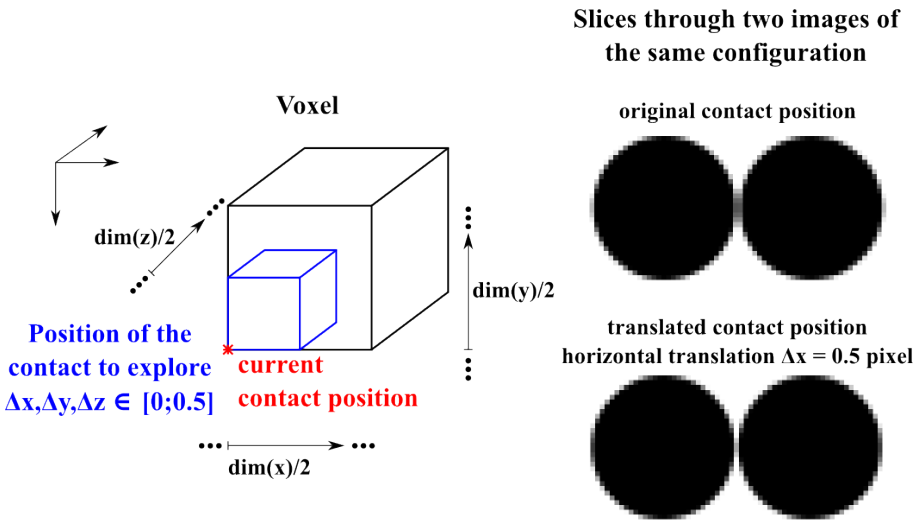

Figure 9: Visualisation of the relative position of the contact in the synthetic images. Left: Indication of the current contact position and the space that can be explored. Right: Effect of the relative contact position. The spheres in both configurations have a distance of 1 pixel, but due to their relative position in the image grid, appear either in contact (top) or not (bottom).

proposed remedial measure is the use of a local threshold which allows the *over-detection distance* to be reduced. In any case, however, this error is due to a *distance*, so it *does not depend on the size of the spheres* and depends only linearly on the pixel size of the image.

Relative position of the contact in the synthetic images. The results presented above are obtained using a fixed position of the contact relative to the image grid, *i.e.*, the geometrical contact point is at exactly the same position in the center of the image for every configuration. The synthetic images are created to have even dimensions (even number of voxels in each dimension) which sets each contact point on the edge of 8 voxels, see the Figure 9 – the red cross indicates the contact position that is considered so far. This raises the question of the importance of the contact position relative to the image grid.

On the right side of the image, the slices of two images of spheres in the same orientation are displayed. The spheres have the same distance in both images. The only difference is that the spheres in the bottom where translated horizontally by half a pixel from their original position. This, however, results in a completely different image – the spheres in the upper image appear in contact whereas the spheres in the lower image do not appear in contact anymore.

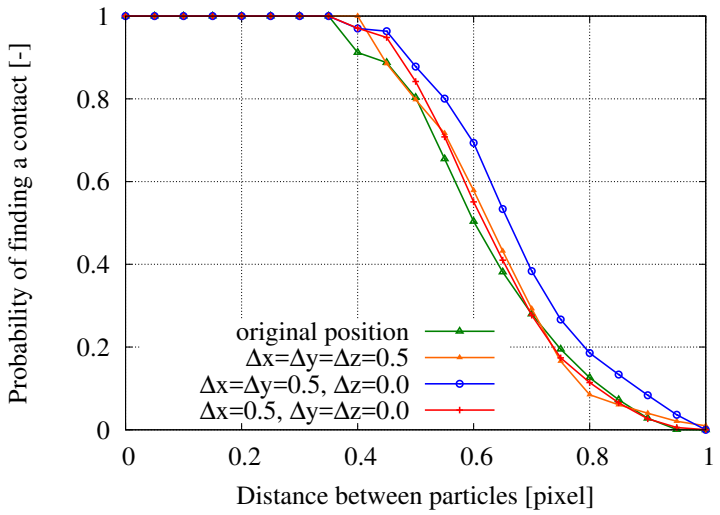

Figure 10: Results of the contact detection study on Kalisphera spheres (diameter = 30 pixels) for different relative positions of the contact in the image grid using a global threshold of 0.5. Results shown for perfect images: no blur and no noise.

In order to study the effect of the relative contact position on the distribution of orientations (see Figure 5) three representative positions were chosen: three corners of the blue box in Figure 9: $\Delta x = \Delta y = \Delta z = 0.5$; $\Delta x = \Delta y = 0.5, \Delta z = 0.0$ and $\Delta x = 0.5, \Delta y = \Delta z = 0.0$. The overall results are shown in Figure 10 and are comparable to the original curve. The relative position of the contact, and thus the spheres appearing in contact, does matter for individual configurations, see Figure 9, but has almost no influence on the overall probability of finding a contact.

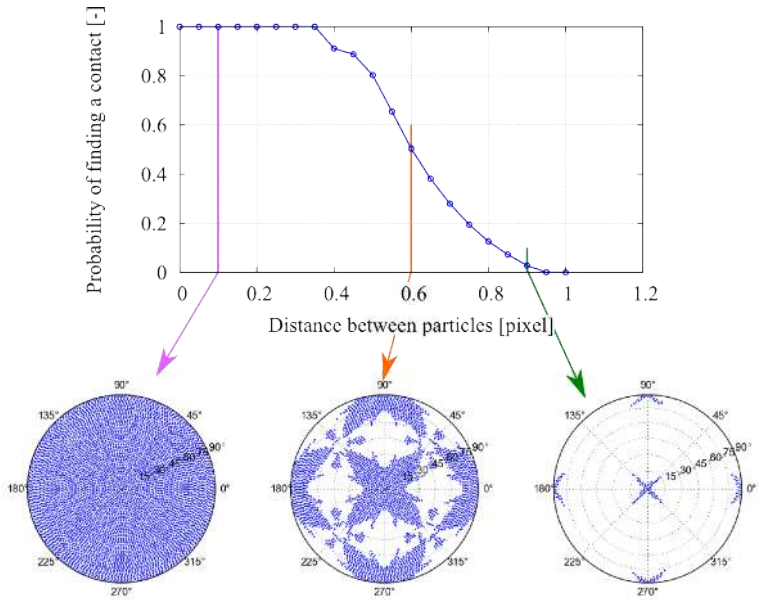

Figure 11: Results of the contact detection study on Kalisphera spheres (diameter = 30 pixels) with a global threshold of 0.5 without applying blur and noise. The Lambert azimuthal equal-area projections show the orientations for which the spheres appear in contact at the indicated distances.

To highlight the influence of the configuration on the *over-detection distance*, the orientations at which the spheres still appear in contact for different distances (0 pixel, 0.6 pixel and 0.9 pixel) are shown in Figure 11. In this case, the image was created without considering blur and noise. The result is shown for the standard position of the contact in the grid and thus, corresponds to the blue line in Figure 7. For this position of the contact in the image grid, the critical orientations are related to 45° to the major axes of the image. This picture changes when different positions of the contact relative to the image grid are considered.

2.3. Contact orientation

When two particles can be said to be in contact, the next step of the analysis requires the orientation of the contact to be measured. In this analysis two touching spheres are used. A global threshold consequently detects a single particle, which is then separated into two objects using a watershed algorithm, allowing each sphere to be given a unique label.

Two different watersheds are investigated herein: a standard interpixel topological watershed [16] (as implemented in [17]) and a more advanced "power watershed" which uses a random walk through the solid phase [18], the Random Walker.

An initial study, limited to binary spheres, of the accuracy of topological watersheds and the more advanced random walker for determining contact orientations is available in [5]. The standard topological watershed was found to introduce a strong bias in the contact orientations of touching spheres, whereas the random walker yields unbiased orientations and significantly lower errors.

In this work we extend the study to more realistic synthetic images, by correctly taking into account the partial volume effect with Kalisphera and by controlling blur and noise. The same types of watersheds studied in [5] are used here. The topological watershed results in a labelled image where the contact area can be defined as the voxels of one label in contact with the voxels of the other label. On the other hand, the random walker generates a probability map (as described in [18]) where each voxel is assigned the probability of belonging to either one of the particles.

Both watershed algorithms are implemented in the skimage package [17] for python. The analysis is carried out on spheres of different sizes for the reference set of orientations.

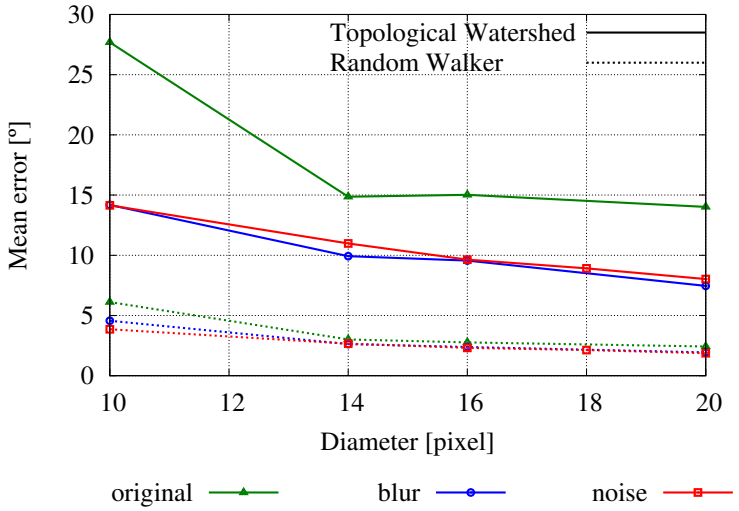

Figure 12: Results of the contact orientation study on Kalisphera spheres. Comparing a topological watershed with the random walker on perfect, blurred and noisy images. The error is defined as the angle between the imposed branch vector and the orientation found by the different watersheds.

For each orientation of our reference set, two touching Kalisphera spheres are generated, and thresholded with the global threshold of 0.5. A plane is fitted through the contact zone using principal component analysis (PCA): for the topological watershed PCA is carried out on the point cloud of two-label contact positions, whereas for the random walker a weighted PCA analysis is carried out on the voxel values either side of the 50% probability line.

The normal to the contact plane represents the contact orientation. As the ground truth of the contact orientation for spheres is by definition the branch vector, the error is defined as the angle between the branch vector and the measured contact orientation. Since the orientation of a contact has no direction associated with it, we establish the convention of choosing the vector that has a positive 3rd component (or z-axis) which facilitates plotting in the projection shown in Figure 5. The mean error for all orientations is plotted against the size of the spheres in Figure 12 for the three cases of the original Kalisphera images (green lines), blurred images (blue lines) and blurred and noisy images (red lines).

Figure 12 indicates that the mean error decreases with increasing sphere size. Furthermore, the addition of blur reduces the mean error (especially for the topological watershed). The introduction of noise on the blurred images yields similar results as the purely blurred images and thus, only has a negligible influence on the contact orientation.

As the size of the spheres increases, in the presence of blur, the number of voxels defining the contact area also increases, resulting naturally in a better fit of the PCA. In the specific case of spheres, the addition of blur increases the size of the contact area, but given the symmetric uniform nature of the spheres, this goes in the direction of adding valuable information to the PCA fit – it is expected with non-spherical shapes that blur will not add valuable information to the fit of the contact area. The main finding of [5] – that the random walker methods have higher performance in this measurement (most probably thanks to the weights it introduces in the PCA) – is clearly confirmed. Furthermore, incorrect over-detected contacts are a particularly bad case of the above.

3. Validation on tomographies of spheres

In order to check whether the findings and refinements on synthetic images also apply to real tomography images at the "standard" resolution for mechanical experiments, high resolution "gold standard" images of different granular materials were acquired using a nano-focus lab x-ray scanner. For consistency with the synthetic images of spheres, manufactured ruby spheres (supplied by Sandoz.ch with a diameter of 400 μm with a tolerance of 0.125 μm sphericity, and of 1 μm on the diameter) are selected. The spheres were scanned in a glass capillary at a pixel size of 1 μm/pixel.

In tomographic scans, unlike in the controlled case of synthetic images, grain centres and radii are not defined *a priori*, meaning that reference distances and orientations are not directly available. These quantities are obtained using a standard watershed and associated processing. The images are binarised using Otsu's threshold [10] and initially segmented using the commercial software Visilog [19], manually repairing oversegmentation. Contacts are defined as the intersection between watershed lines in the binarised image, and are associated to contacting grains. Totally 137 contacts were found. In the subsequent analyses only 99 of these contacts are retained, since the others include grains that lie on the boundary of the image.

Downscaling gold standard images realistically. The original 1 μm/pixel images serve as a gold standard for the analysis of contact detection and orientation for the lower resolution experimental scale. Gold standard images are scaled down to 5-20 μm/pixel with simple rebinning, whilst keeping the original (high resolution) information of grain centres. However the resulting images are not representative of the tomography images (of many particles) acquired at the lower resolution, in that they have a much lower degree of noise and blur due to rebinning. Controlled noise and blur is therefore added back to the downscaled images artificially, following a procedure outlined in Figure 13 operating on pairs of touching particles.

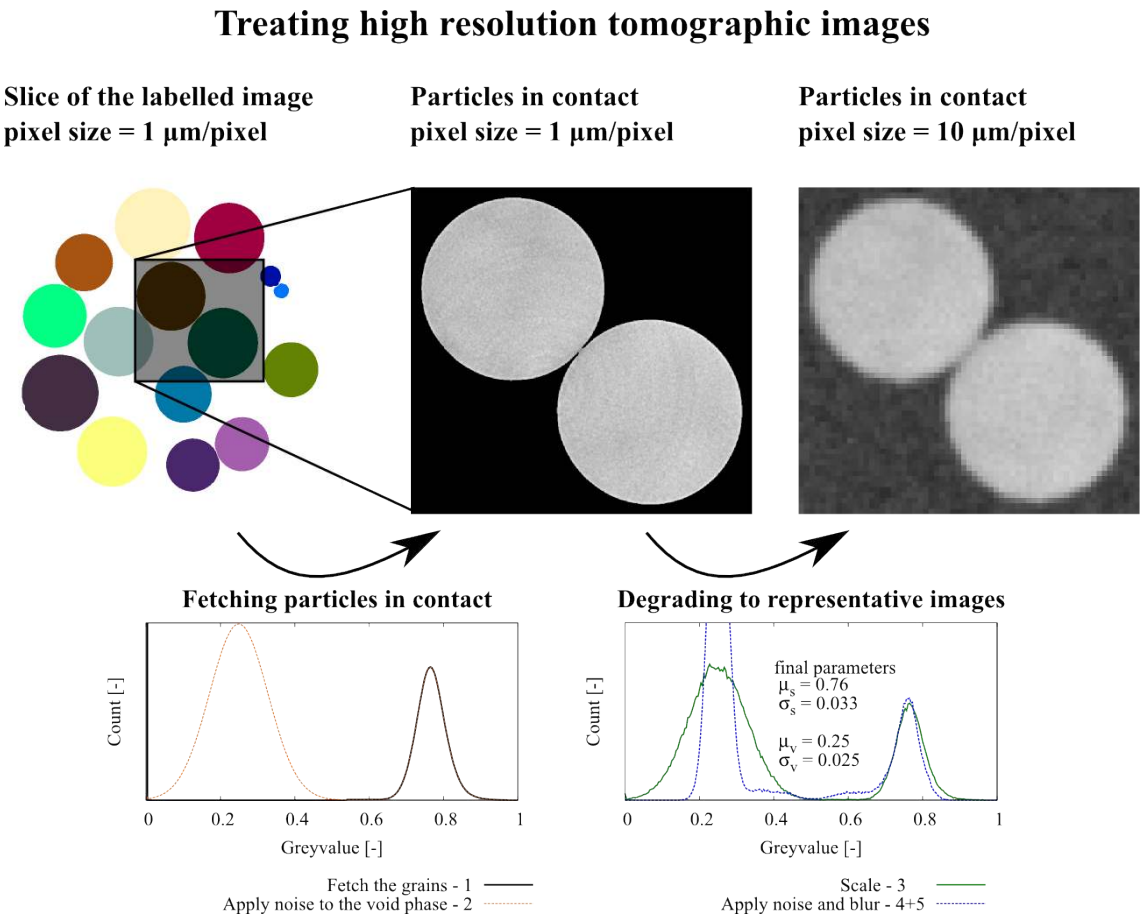

Figure 13: Dealing with the high resolution images for the analysis on contact detection and orientation. 1. Fetch the particles in contacts from the labelled image. 2. Apply noise to the void space at the original pixel size. 3. Scale down. 4. Add blur. 5. Apply noise to the whole image.

In the first step only the greyscale voxels of the two particles in contact are fetched (from the labelled image). In the resulting image (center image in the Figure) the void space is empty (greyvalue=0), whereas the solid phase has a distribution of greyvalues corresponding to the original noise in the 1 μm/pixel scan. The void space is set to a greyvalue of 0.25 (following the standard set before) and random noise is added in accordance with the noise of the solid phase. The image is subsequently scaled to the prescribed pixel size using the scipy [20] function zoom `ndimage.interpolation.zoom` with linear interpolation. Since the original images have a low level of blur and noise, blur and random noise are added after the scaling to obtain realistic images corresponding to usually lower resolutions. The noise is calibrated to yield similar standard deviations of the histograms compared to the experimental images described in Figure 4.

3.1. Contact detection

The approach to determine the accuracy of the contact detection analysis – *i.e.*, the overdetection distance – is in the same spirit as the analysis on the synthetic images above. The analysis is carried out at pixel sizes equal to 5, 10, 15 and 20 μm/pixel on the 99 contacts. As before, the analysis starts with a distance of 0 μm between two particles, which is increased subsequently until the particles do not appear to be in contact anymore. For each of these distances, different local thresholds are applied to the greyscale image.

Particles are moved apart in pixel increments in the high resolution image, which is then downscaled as described above (for example for a 20x downscale giving a pixel size of 20 μm/pixel, a 1 pixel displacement at high resolution corresponds to a 0.05 pixel in the final image). Displacements are applied in the direction of the branch vector.

The increment of translation is not necessarily identical to the distance between the particles: with natural, non-convex shapes (such as Hostun sand, which will be discussed later) the branch vector and the normal to the surface very rarely coincide. Thus, the minimal distance between the two particles is calculated at each step of this analysis, by looking for the minimal Euclidean distance between surfaces using a k-dimensional binary tree as implemented in [20].

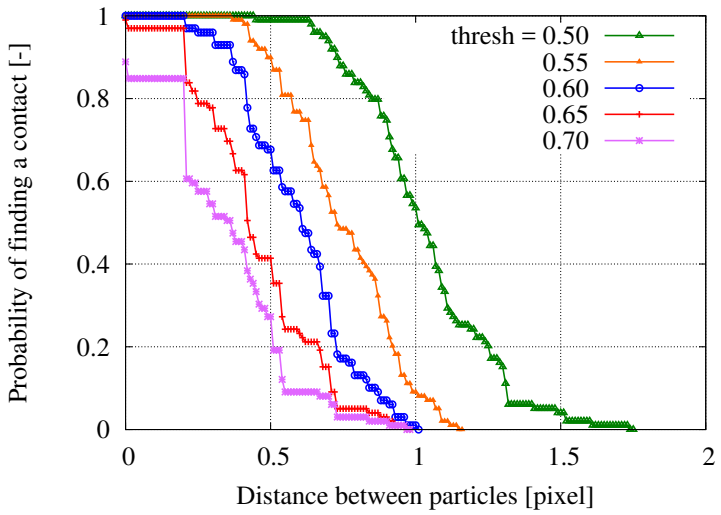

Figure 14: Results of the contact detection study on the manufactured spheres at a pixel size of 10 μm/pixel using a global threshold of 0.5 and applying different local thresholds.

The results of the analysis on the manufactured spheres are plotted in Figure 14 for a pixel size of 10 μm/pixel. The green line shows the error that is encountered using the standard approach with a global threshold of 0.5. Higher local thresholds improve the contact detection substantially, but care must be taken when adjusting them. In this case, contacts start to get lost at a threshold of 0.70 for zero distance, which is earlier than for the synthetic images.

The repetition of this analysis at different pixel sizes (shown in Figure 15 for the manufactured spheres) confirms the finding on synthetic images that contact detection using the global threshold is resolution-independent. The results of different local thresholds, however, vary with the scale and thus, the optimal local threshold is different for each level of zoom – it increases with decreasing pixel size (not shown here).

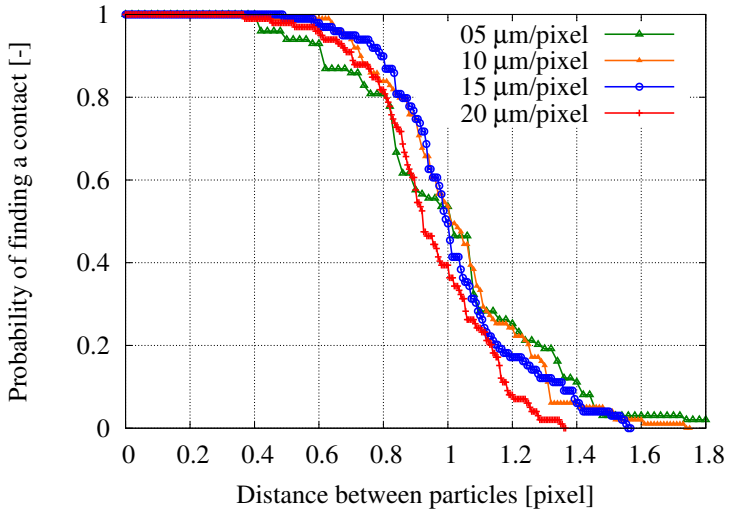

Figure 15: Results of the contact detection study on the manufactured spheres at various pixel sizes using a global threshold of 0.5.

3.2. Contact orientation

The analysis of contact orientation follows again a similar approach as for the synthetic images of spheres. A contact orientation is determined at various levels of zoom using two different watershed methods: the interpixel topological watershed and the random walker; the error is defined as the angle between this contact orientation and the reference orientation, as defined above. Exploiting the spherical shape, the reference contact normal orientation is set to be the orientation of the branch vector.

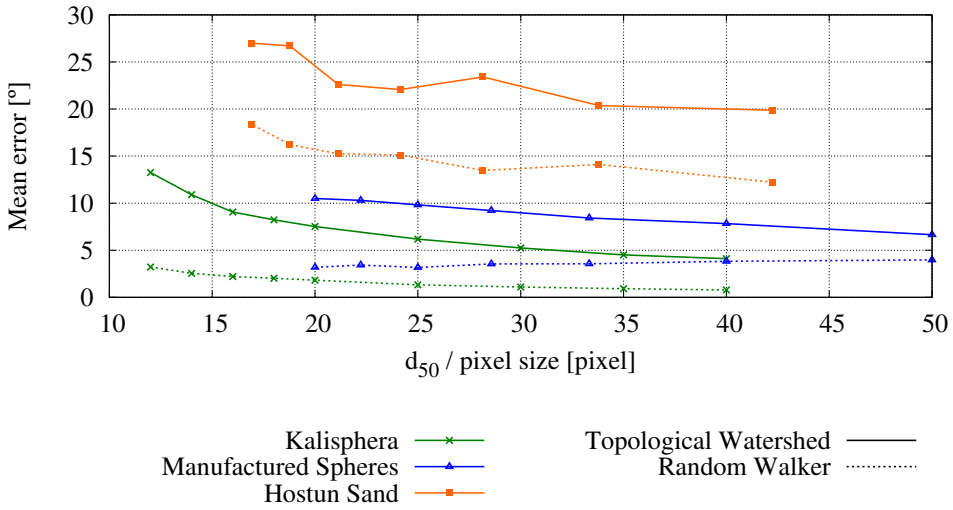

Figure 16: Results of the contact orientation study on the high resolution tomographic images of the manufactured spheres (blue lines) and Hostun Sand (orange lines) for the topological watershed (solid lines) and the random walker (dotted lines). The results of the study on synthetic images of spheres in contact are added for comparison (green lines).

The results of the analysis on the manufactured spheres are plotted with blue lines in Figure 16. The trend for the topological watershed is similar to the trend for synthetic images of spheres (plotted with green lines): the smaller the size of the particles in pixels (or rather the lower the pixel size with constant particle size), the higher the mean error. In the range studied here, the error of the random walker stays relatively constant at 3-4° with increasing mean size of the particles. This is in agreement with the findings for the synthetic images, see Figure 12. Again, the random walker yields lower mean errors and should thus be the segmentation algorithm of choice when orientations are to be determined.

4. Natural sand

After validating the findings of the study on spheres (both synthetic and real), the same procedure is applied to grains of Hostun sand, a reference natural material in soil mechanics research. This is an angular sand where 50% of the mass passes through a sieve opening of 338 μm (D_{50} in soil mechanics terminology). Figure 17 shows clearly that Hostun grains are far from spheres and have complex surfaces giving complex grain-to-grain contacts. 1μm/pixel gold standard images were also acquired of this material.

After undergoing the same initial treatment, as described in the previous section, 196 contacts were detected in the original images and 135 were retained.

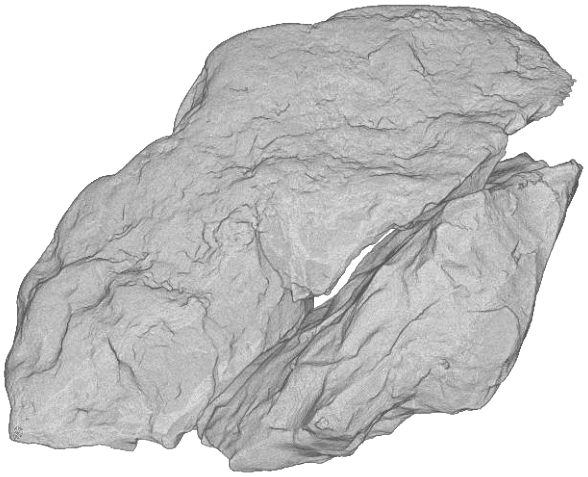

Figure 17: 3D rendering of a complex contact between two grains in Hostun sand. The two grains are touching at multiple locations.

4.1. Contact detection

Repeating the *over-detection distance* analysis at 10 μm/pixel yields the results shown in Figure 18. Again, the green line is obtained using a global threshold of 0.5. The effect of the local threshold on contact detection is significantly different from the results on spheres with two trends immediately noticeable:

1. The *over-detection distance* for the 0.50 threshold is significantly reduced, with a 50% chance of overdetection at around 0.6 pixels separation, to be compared to 1.0 pixel for real spheres and more for synthetic ones.
2. For small increases of the local threshold contacts are immediately lost, meaning that under-detection is possible.

This significant difference can be interpreted as a strong manifestation of the natural shape of the grains, and more specifically, the possibility of "sharp" point-like contacts which are impossible between spheres. Especially for sharp contact topologies (as visible in Figure 17), the scaling and the translation of the grains can lead to a severe loss of greyvalue in the contact area, due to the large amount of void close to these contacts.

4.2. Contact orientation

For Hostun sand with its natural grain shapes the reference orientation cannot be derived geometrically from the grain shape, thus a choice was made to take the gold standard watershed line as the reference orientation (another choice could be some local measurement of surface normal in the vicinity of the contact). In order to determine this reference orientation, a contact plane is fitted on the contact area in the labelled image.

Figure 16 shows the results of the contact orientation analysis on Hostun sand with orange lines. The mean errors of both the topological watershed and the random walker, follow the same trend that was found in the previous analyses: they decrease with increasing pixel size/mean particle size. Again, the random walker yields a lower mean error with $\approx 15^\circ$ compared to the topological

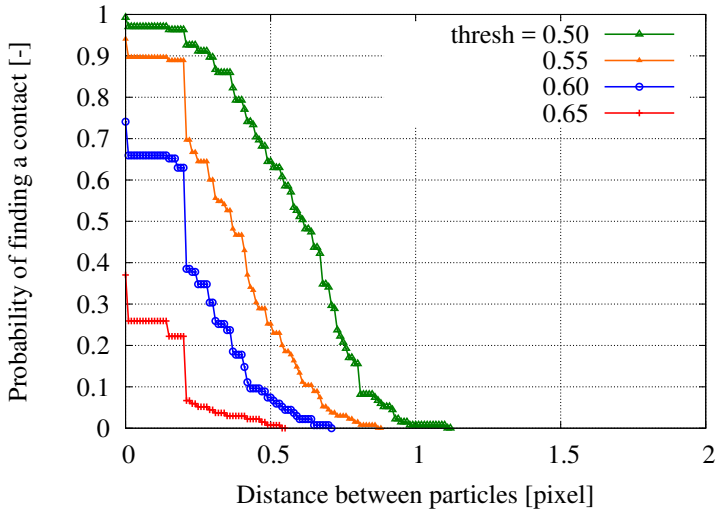

Figure 18: Results of the contact detection study on Hostun sand at a degraded pixel size of 10 μm/pixel using a global threshold of 0.5. Applying different local thresholds.

interpixel watershed with 20-27°. However, the error of both segmentation algorithms is higher than that encountered with spheres. The uncertain definition of the reference orientation may have some role to play in the increased error, however the non-symmetrical nature of the contact combined with the fact that sharp contacts by definition "cross" fewer voxels necessarily increases errors in both techniques.

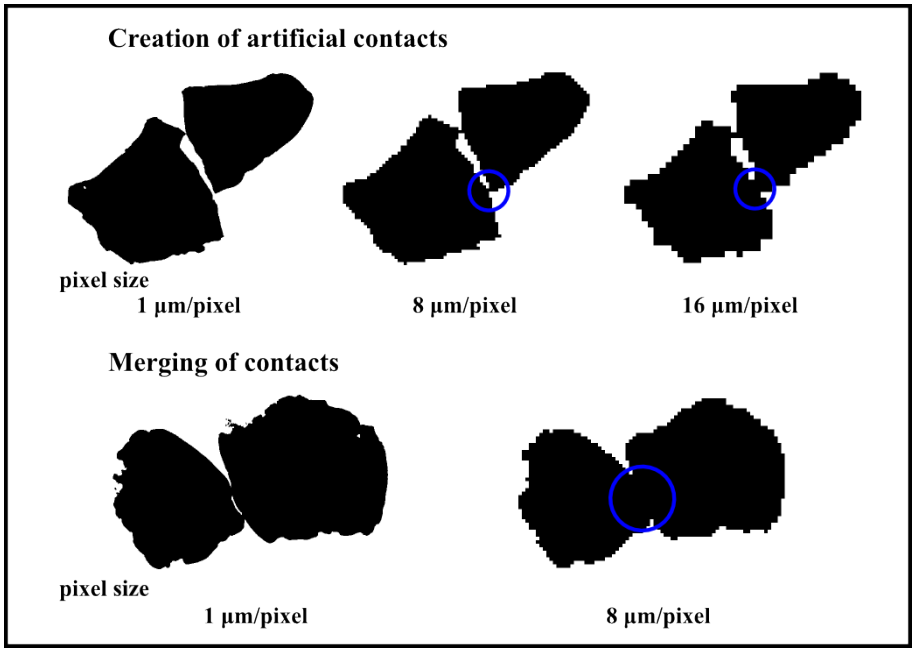

Figure 19: Artificial creation of contacts due to scaling.

When reducing the pixel size of images, apparent contact points can be created as shown in Figure 19. The figure presents two slices through pairs of grains (on two different rows) that have either one or two individual contact points in the gold standard image. Images with degraded pixel size are shown on the right, illustrating how contacts can either appear or grown in size. Apparent contacts arise on downscaling when grains are sufficiently close for their partial volume effects to overlap. At the original pixel size of 1 μm/pixel the contact in the upper image consists of a few voxels only, resulting in a weak fit (PCA) for the reference orientation, which is a first indicator of error-prone orientations.

5. Conclusions and perspectives

In the mechanics of granular media, interparticle contacts play a fundamental role, and in fact may encode the essence of the grain-scale behaviour. X-ray tomography has proven to be a very precious tool for investigating grain-scale mechanics, with a number of works measuring grain kinematics, as well as some studies reporting quantities related to grain contacts. However, unlike particle kinematics, to the best of our knowledge no metrological study of contact properties from x-ray tomography images of particles has ever been undertaken in a rigorous manner – in particular for images from mechanical experiments with many particles and limited spatial resolution (only tens of voxels across each particle). This paper quantifies the accuracy of the *detection* of contacts from tomography images, and once detected the accuracy with which their *orientation* can be measured by means of the most common techniques used in the imaging of granular materials. To this end, this paper provides a "golden standard" procedure to study the accuracy of image processing techniques to determine contact properties in granular materials.

Three cases of increasing complexity are studied: Synthetic 3D images of spheres, real tomographies of spheres and real tomographies of natural, angular sand grains. Only the first case allows perfect control of both the particles (their positions and size) as well as image defects (noise and blur). To remedy this, very high resolution "gold standard" images of a few particles are used as a geometrical reference.

Contact detection. We find that if particles are defined using a greyscale threshold that selects the correct solid volume (a common and logical choice), then contacts are systematically over-detected. This means that two particles that are close but not in contact can appear to be in contact – the non-zero distance at which this appears is called the *over-detection distance*. There is good accordance between the two data sets on spheres: the *over-detection distance* increases strongly with blur (intended as the point-spread function of the imaging system) and for normal levels of blur a systematic *over-detection distance* of 1 pixel is found. Noise further increases the *over-detection distance*, although less strongly (within reasonable values) than the blur. The natural grain data set also exhibits an *over-detection distance*, but to a lesser extent (around 0.6 pixels).

For the case of spheres, we propose an increased *local threshold* intended only to check whether particles are really in contact: this allows the *over-detection distance* to be reduced by about half. Due to the sharper contact points possible in the angular grains, this concept does not work when applied to all contacts, since real contacts might get lost with even small increases of the threshold.

Contact Orientation. For spheres contact orientations can be very accurately obtained from branch vectors (the vector joining the grain centers), however with any departure from a sphere this no longer holds.

Using standard techniques for separating thresholded grains, we confirm the findings of [5], *viz.* significant *mean* errors in contact orientation when using the subtracted "watershed line" as the geometrical definition of the contact. We find that the mean error decreases with decreasing pixel size (*i.e.*, more voxels per particle), a justification for doing experiments at higher resolution. A significant reduction in mean error is obtained by using a "Random Walker" segmentation algorithm, which assigns a probability to each voxel of belonging to either one of the particles in contact. Using these probabilities a 50% surface can be interpolated at sub-pixel resolution that represents the contact plane. Interestingly, adding blur helps to reduce the watershed line technique's mean error, which is explained by the fact that contacts are symmetric and grow in size with blur, meaning that a better fit can be made. In the case of complex and non-symmetric contacts in natural materials, the contact orientations are defined with fewer voxels, meaning poorer fits and furthermore, considering the sometimes non-convex shapes of particles virtual contacts can appear, changing the measured orientation. For the case that interests us in particular (D_{50}/pixel size around 20) the mean error can be as high as 22° for standard techniques, which is improved to 15° with a random walker (to be compared to a few degrees for spheres).

Perspectives. This paper has shown that correct quantification of interparticle contacts from x-ray tomographies is not trivial. The obvious perspectives of this work is to extend this study to the large range of different possible natural grain shapes between the two extreme examples of spheres and very angular sand grains. Practically speaking the reference materials of Ottawa sand or Toyoura sand come to mind.

The partial results on contact detection and orientation of spherical particles might contribute to the field of granular physics where research focusses principally on rather perfectly rounded shapes, see *e.g.*, [21]. However, little work has been done on natural, angular particles so far.

Another clear conclusion of this work is that the definition of contact orientations coming from the segmentation has a number of problems, which are not significantly relieved with increased resolution. An interesting perspective is to consider the definition of contact orientation as a mean orientation of the local surface normal of the two grains in contact; this may decrease error, although point-to-plane like contacts will have to be detected and treated specifically. Levels sets also present an alternative – although perhaps too smooth – to this problem [13].

A final and more general perspective clearly relates to the *use* of these measurements in geomechanics research: the obvious candidate is the measurement of contact-based granular fabric, where a comprehensive study of the effect of the highlighted errors in both detection and measured orientation is essential. One avenue currently under investigation is the use of discrete element simulations to make small and controlled changes to contact fabric.

6. Acknowledgments

We express our thanks to Alessandro Tengattini for creating Kalisphera (with Edward Andò) and sharing it with the research community and Félix Bertoni for implementing it in C++. Furthermore, we would like to thank Itai Einav, François Guillard and Takashi Matsushima for enriching discussions and opening new questions.

The research leading to these results has received funding from the German Research Foundation (DFG) n° HE2933/8-1 and from the European Research Council under the European Union's Seventh Framework Program FP7-ERC-IDEAS Advanced Grant Agreement n° 290963 (SOMEF). Laboratoire 3SR is part of the LabEx Tec 21 (Investissements d'Avenir - grant agreement n°ANR-11-LABX-0030).

References

[1] M Oda. Initial fabrics and their relations to mechanical properties of granular material. *Soils and Foundations*, 12(1), 1972.

[2] M Oda, S Nemat-Nasser, and J Konishi. Stress-induced anisotropy in granular masses. *Soils and Foundations*, 25(3):85–97, 1985.

[3] Alessandro Tengattini and Edward Andò. Kalisphera: an analytical tool to reproduce the partial volume effect of spheres imaged in 3D. *Measurement Science and Technology*, 26(9), 2015.

[4] E. Andò, G. Viggiani, S. a. Hall, and J. Desrues. Experimental micro-mechanics of granular media studied by x-ray tomography: recent results and challenges. *Géotechnique Letters*, 3:142–146, 2013.

[5] Clara Jaquet, Edward Andó, Gioacchino Viggiani, and Hugues Talbot. Estimation of Separating Planes between Touching 3D Objects Using Power Watershed. In *International Symposium on Mathematical Morphology*, volume 11, pages 452–463, 2013.

[6] Pavel Iassonov, Thomas Gebrenegus, and Markus Tuller. Segmentation of X-ray computed tomography images of porous materials: A crucial step for characterization and quantitative analysis of pore structures. *Water Resources Research*, 45(9):1–12, 2009.

[7] V. Cnudde and M. N. Boone. High-resolution X-ray computed tomography in geosciences: A review of the current technology and applications. *Earth-Science Reviews*, 123:1–17, 2013.

[8] S. Ontiveros, J. A. Yagüe, R. Jiménez, and F. Brosed. Computer tomography 3D edge detection comparative for metrology applications. *Procedia Engineering*, 63(2010):710–719, 2013.

[9] Axelle Amon, Philip Born, Karen E. Daniels, Joshua A. Dijksman, Kai Huang, David Parker, Matthias Schröter, Ralf Stannarius, and Andreas Wierschem. Preface: Focus on imaging methods in granular physics. *Review of Scientific Instruments*, 88(5), 2017.

[10] Nobuyuki Otsu. A Threshold Selection Method from Gray-Level Histograms. *IEEE Transactions on Systems, Man, and Cybernetics*, 9:62–66, 1979.

[11] Simon Weis and Matthias Schröter. Analyzing X-Ray tomographies of granular packings. *Review of Scientific Instruments*, (88), 2017.

[12] Joerg Reimann, Jerome Vicente, Emmanuel Brun, Claudio Ferrero, Yixiang Gan, and Alexander Rack. X-ray tomography investigations of mono-sized sphere packing structures in cylindrical containers. *Powder Technology*, 318(July):471–483, 2017.

[13] Ivan Vlahinić, Reid Kawamoto, Edward Andò, Gioacchino Viggiani, and José E. Andrade. From computed tomography to mechanics of granular materials via level set bridge. *Acta Geotechnica*, 12:85–95, 2017.

[14] G. Kerckhofs, J. Schrooten, T. Van Cleynenbreugel, S. V. Lomov, and M. Wevers. Validation of x-ray microfocus computed tomography as an imaging tool for porous structures. *Review of Scientific Instruments*, 79(1), 2008.

[15] Edward Andò. *Experimental investigation of microstructural changes in deforming granular media using x-ray tomography.* PhD thesis, Université de Grenoble, 2013.

[16] S. Beucher and C. Lantuejoul. Use of watersheds in contour detection. In *International Workshop on image processing: Real-time image and Motion detection/estimation, Rennes, France*, 1979.

[17] Stéfan van der Walt, Johannes L. Schönberger, Juan Nunez-Iglesias, François Boulogne, Joshua D. Warner, Neil Yager, Emmanuelle Gouillart, Tony Yu, and the scikit-image contributors. scikit-image: image processing in Python. *PeerJ*, 2:e453, 6 2014.

[18] Leo Grady. Random walks for image segmentation. In *IEEE Transactions on Pattern Analysis and Machine Intelligence*, volume 28, 2006.

[19] L Bernard, S Fave, E Noirfalise, and A Saragaglia. Visilog 7 reference guide, 2011. Manual.

[20] Eric Jones, Travis Oliphant, Pearu Peterson, et al. SciPy: Open source scientific tools for Python, 2001–.

[21] Schröter, Matthias. A local view on the role of friction and shape. *EPJ Web Conf.*, 140:01008, 2017.